TU Delft

Delft University of Technology

Experimental results on a hydrostatic bearing lubricated with a magnetorheological fluid

Lampaert, S. G.E.; van Ostayen, R. A.J.

DOI
10.1016/j.cap.2019.09.004

Publication date
2019

Document Version
Final published version

Published in
Current Applied Physics

Citation (APA)
Lampaert, S. G. E., & van Ostayen, R. A. J. (2019). Experimental results on a hydrostatic bearing lubricated with a magnetorheological fluid. *Current Applied Physics*, *19*(12), 1441-1448. https://doi.org/10.1016/j.cap.2019.09.004

Important note
To cite this publication, please use the final published version (if applicable).
Please check the document version above.

Copyright
Other than for strictly personal use, it is not permitted to download, forward or distribute the text or part of it, without the consent of the author(s) and/or copyright holder(s), unless the work is under an open content license such as Creative Commons.

Takedown policy
Please contact us and provide details if you believe this document breaches copyrights.
We will remove access to the work immediately and investigate your claim.

This work is downloaded from Delft University of Technology.
For technical reasons the number of authors shown on this cover page is limited to a maximum of 10.

Current Applied Physics 19 (2019) 1441–1448

Contents lists available at ScienceDirect

Current Applied Physics

journal homepage: www.elsevier.com/locate/cap

Experimental results on a hydrostatic bearing lubricated with a magnetorheological fluid

S.G.E. Lampaert*, R.A.J. van Ostayen

Department of Precision and Microsystems Engineering, Delft University of Technology, Mekelweg 2, 2628CD, Delft, the Netherlands

ARTICLE INFO

Keywords:
Hydrostatic bearing
Magnetorheological fluid
Bingham plastic
Mathematical modelling
Magnetics

ABSTRACT

Magnetorheological fluids can be used as a smart lubricant as a result of the fact that its properties can be changed with the use of a magnetic field. Local flow resistance and local pressure can be generated by applying a local magnetic field. This work presents a hydrostatic bearing in which the pressure profile of a conventional hydrostatic bearing is recreated with solely the use of a magnetic field and a magnetorheological fluid. The magnetic field is applied only locally at the outer edges of the bearing with the use of an electromagnet. The principle is demonstrated with the use of an experimental setup and a model from literature.

1. Introduction

The bearing has made a lot of progress since its inception, and the typical lifetime has increased considerably combined with a significantly reduced friction [1,2]. Still the system is not perfect, and the cost of energy losses due to friction and system failure for society are still huge. In addition, the CO_2 emissions due to friction are especially important nowadays. Estimations show that in total about 23% (119 EJ) of the world's total energy consumption is caused by tribological contacts [3].

One way to improve bearings systems even further be may be with the use of smart fluids. Examples exist that use the addition of magnetic fields together with ferrofluids [4–7] and magnetorheological (MR) fluids [8–17] to boost the performance. Other examples exist that use the addition of electric field together with electrorheological (ER) fluids to boost the performance [18–21].

The common property of these MR and ER lubricated bearings is that the variable rheological properties of the lubricant add an extra design variable to the system. This extra variable opens up a completely new dimension of bearing configuration. Conventional bearing system use local changes in the bearing surface geometry, so called local textures, to create a local change in flow resistance. Bearing systems using MR fluids can create that local change by the application of local magnetic fields, so called MR textures [22–26].

This research demonstrates the potential of this MR texturing by demonstrating the similarities of a hydrostatic bearing using only geometrical surface textures and a hydrostatic bearing using only MR textures (Fig. 1). An experimental setup, a numerical and an analytical model show the load capacity in function of the fluid film height. This work furthermore shows the potential of the manipulation of the magnetic field to facilitate active control of the bearing properties.

2. Method

Three different methods demonstrate the behaviour of a hydrostatic bearing with MR texturing in this paper. Firstly, an experimental setup is built that is able to measure the load capacity in function of the fluid film height. Secondly, a numerical model is built that simulates the behaviour of the experimental setup as closely as practically possible. Lastly, an analytical model from literature simulates this same situation in a more approximate but time efficient way. Fig. 1 presents the different geometrical parameters used throughout this research.

2.1. Syntheses of the fluid

The MR fluid used in the experiments consists of a mixture of a low viscosity mineral oil (Shell Tellus S2 VX 15) with oleic acid (OA) and fine iron particles (BASF Carbonyl Iron Powder HS, $d_{part} = [1.8 - 2.3]\mu m$). The OA has as function to put the particles easily back into suspension. At rest the particles will slowly settle at the bottom due to the large size of the particles [27]. OA makes this sediment soft and easy to mix again, the absence of OA makes the sediment very hard and almost impossible to mix back into suspension. The substances are mixed in a mass ratio of $\varphi_{iron} = 0.720 kg/kg$, $\varphi_{oil} = 0.228 kg/kg$, $\varphi_{OA} = 0.0520 kg/kg$ into a total mixture of $m_t = 5.48 kg$. The mixture is stirred for 24 h, first by hand, later by using a

* Corresponding author.
E-mail address: S.G.E.Lampaert@tudelft.nl (S.G.E. Lampaert).

https://doi.org/10.1016/j.cap.2019.09.004
Received 8 March 2019; Received in revised form 25 July 2019; Accepted 5 September 2019
Available online 21 September 2019
1567-1739/ © 2019 The Authors. Published by Elsevier B.V. on behalf of Korean Physical Society. This is an open access article under the CC BY license (http://creativecommons.org/licenses/BY/4.0/).

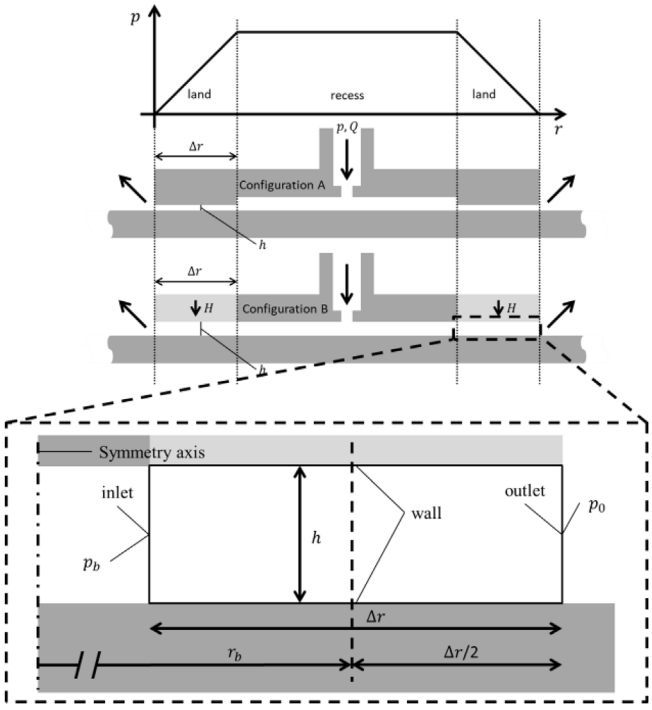

Fig. 1. A set of magnets mimics a geometrical surface structure Only the outer rim has a magnetic field such that the fluid experiences only resistance at the outer rim of the bearing resulting in a declining pressure there.

mechanical mixer.

Constant mixing was present in the lubricant reservoir during the experiments to minimize the sedimentation. Still some sedimentation occurred. For this reason, a density measurement is performed during the bearing measurements by taking samples $V_{samp} = 0.1ml$ of lubricant with a micropipette and measuring its weight. The density is measured with a set of 20 measurements that lead to a mean density of $\rho_{lub,exp} = 1{,}94kg/l$ with a standard deviation of $0{,}24kg/l$. This density is significantly lower than the expected density of $\rho_{lub,ini} = 2{,}38kg/l$. From these numbers it is assumed that the realised content of the iron is $\varphi_{iron,exp} = 0.63kg/kg$ or $\delta_{iron,exp} = 0.15l/l$.

2.2. Material properties

Table 1 presents the susceptibility and saturation magnetization of different carbonyl iron (CI) particles found in literature. The work of [28] presents the material properties of the same CI particles as used in this research The particles have a magnetic permeability of $\mu_i = 1 - \chi \approx 3.5$ and an assumed saturation magnetization of $M_{s,CI} = 1600kA/m$. The Maxwell-Garnett relation given in (EQ (1)) describes the effective permeability of the MR fluid [29]. The saturation magnetization scales with the volumetric particle concentration of the fluid which results in a saturation magnetizing of $M_s = 240$kA/m or $B_s = 0.3$T(EQ2) [30–34].

Table 1
Susceptibility and saturation magnetization of CI particles.

$d_{part}\,[\mu m]$	χ	$M_{s,CI}\,[kA/m]$	Source
1	20.46 ± 0.19	1700	[35]
2	5	1600	[36]
2	2.53	n.a.	[28]
2.8 − 3.5	4.76	1500	[37]
1	5	1700	[38]

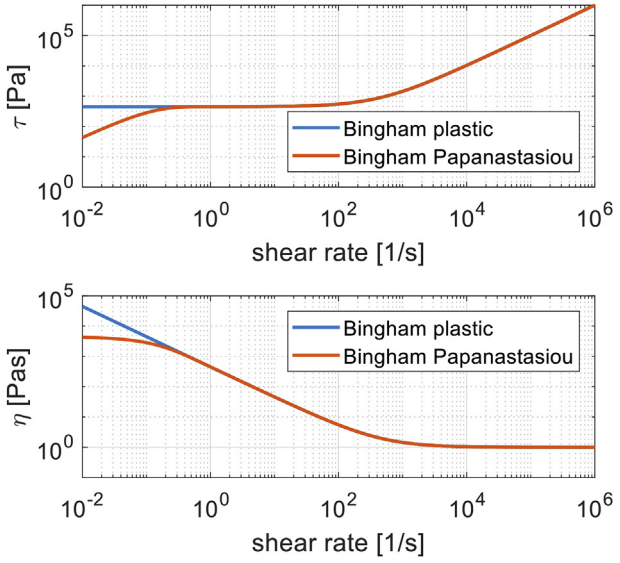

Fig. 2. Comparison between the Bingham plastic fluid model and the Bingham-Papanastasiou model used in the numerical computation.

$$\mu_{eff} = \frac{2\delta_{iron,exp}(\mu_i - 1) + \mu_i + 2}{\delta_{iron,exp}(1 - \mu_i) + \mu_i + 2} = 1.22 \tag{1}$$

$$M_s = \delta_{iron,exp} M_{s,CI} = 240kA/m \tag{2}$$

A Bingham plastic fluid model (EQ (3)) approximates the viscous behaviour of the MR fluid [39]. Here both the yield stress and the viscosity are a function of the magnetic field intensity. The drawback of this model is that it gives some difficulties during numerical simulation as a result of the non-zero yield stress at zero shear rate. Using the Bingham-Papanastasiou model (EQ (4)) solves this since that approximates the behaviour of the yield stress by generating a very high viscosity at low shear rates [40,41]. A regularization parameter m is chosen such that he the Bingham-Papanastasiou model follows the Bingham plastic model down to a shear rate of $\dot{\gamma} = 1s^{-1}$. Shear rates lower than $\dot{\gamma} = 1s^{-1}$ are assumed to be of negligible influence to the solution. Fig. 2 presents the Bingham plastic model and the Bingham-Papanastasiou model for a yield stress present at M2 of Table 2 in function of a range of relevant shear rates. A regularization parameter of $m = 10$ is chosen such that the Bingham-Papanastasiou model closely follows the Bingham plastic model down to a shear rate of $\dot{\gamma} = 1s^{-1}$.

$$\eta = \eta_0 + \frac{\tau_y}{|\dot{\gamma}|} \tag{3}$$

$$\eta = \eta_0 + \frac{\tau_y}{|\dot{\gamma}|}\left(1 - e^{-m|\dot{\gamma}|}\right) \tag{4}$$

There are different methods to measure the properties of yield stress fluids [42,43]. In this research, a commercial cone-plate viscometer (Anton Paar MCR302) measures the viscous behaviour of the fluid. The viscous behaviour as a function of shear rate and magnetic field is measured. The shear rate is measured in a range from $\dot{\gamma}_{low,mes} = 0.1s^{-1}$ to $\dot{\gamma}_{high,mes} = 100s^{-1}$. The magnetic field is measured in a range from

Table 2
Measurement specific parameter values.

Parameter	Symbol	Value M0	Value M1	Value M2	Unit
Current	I	0	1	2	*A*
Pressure	p_s	4×10^5	4×10^5	3×10^5	*Pa*
Average yield stress,	$\tau_{yield,avg}$	0	160	450	*Pa*
Viscosity	η	0.073	1	3	*Pa s*
Number of measurement sets	N_{sets}	7	9	5	–

Table 3
General parameter values of the experimental setup.

Parameter	Symbol	Value	Unit
Bearing radius	r_b	0.02	m
Inner cavity	r_0	0.0025	m
Length of land	Δr	0.01	m
Restrictor	R_s	8.3×10^{11}	$Pas/m\hat{}3$
Saturated yield stress	$\tau_{y\infty}$	3355	Pa
Starting yield stress	τ_{y0}	10	Pa
Saturation speed	$\alpha_{s\tau_y}$	0.0056	T^{-1}
Saturated viscosity	η_∞	10	Pas
Starting viscosity	η_0	0.073	Pas
Saturation speed	$\alpha_{s\eta}$	0.01	T^{-1}

$B_{low,mes} = 0mT$ to$B_{high,mes} = 645mT$. The measurement is done six times for each combination of shear rate and magnetic field. The shear rate range is relatively low due to high thermal dissipation in combination with a high magnetic field strength; the cooling system was not able to cool the fluid properly causing inaccurate results. The magnetic field was measured up to the saturation point of the fluid [44]; the yield stress did not increase further from this point. A fluid sample is taken from the fluid reservoir of the experimental setup during the measurement of the load curve. This made sure that the same fluid properties are measured as present during the load curve measurement.

The Bingham model defines the fluid behaviour in the numerical modelling of the bearing behaviour [34]. The parameters of the Bingham model are fitted to the data measured with the rheometer [45]. This leads to one specific yield stress and one specific viscosity for every measured flux density. The functions presented in (EQ (5)) and (EQ (6)) are fitted to the different yield stresses and viscosities such that the complete rheological behaviour is turned into an analytical relation in function of the magnetic field and the shear rate [46]. See Table 3 for the explanation of the different parameters.

$$\tau_y = \tau_{y\infty} + 2(\tau_{y0} - \tau_{y\infty})\left(e^{-\alpha_{s\tau_y}B} - 0.5e^{-2\alpha_{s\tau_y}B}\right) \tag{5}$$

$$\eta_y = \eta_\infty + 2(\eta_0 - \eta_\infty)\left(e^{-\alpha_{s\eta}B} - 0.5e^{-2\alpha_{s\eta}B}\right) \tag{6}$$

Fig. 3 presents three shear stress vs shear rate measurements performed on the fluid. The points present the different measurements and the solid line presents the resulting fit of that measurement. Fig. 4 presents the fit values of all the viscosity measurements done.

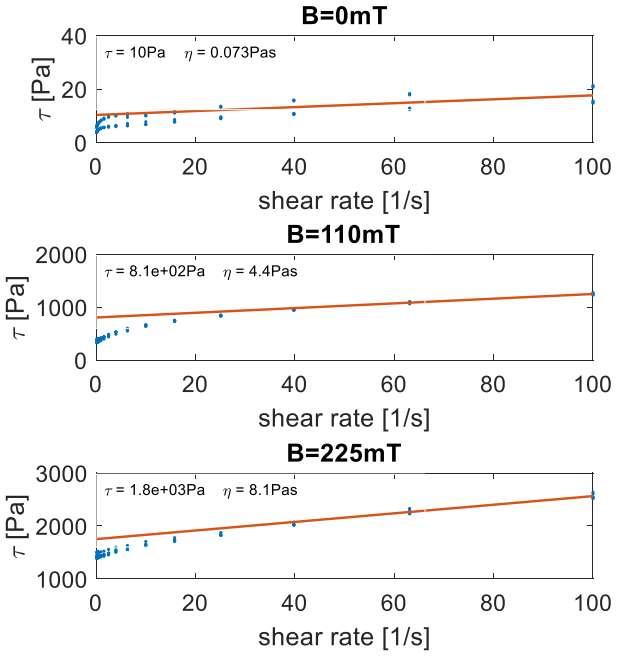

Fig. 3. Three viscosity measurement for different magnetic fields.

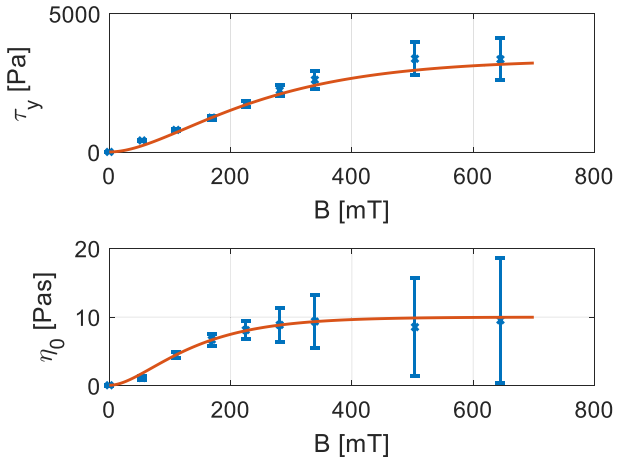

Fig. 4. Yield stress and viscosity values fitted to the viscosity measurements and used in the Bingham model. The confidence interval of the fit is 90%.

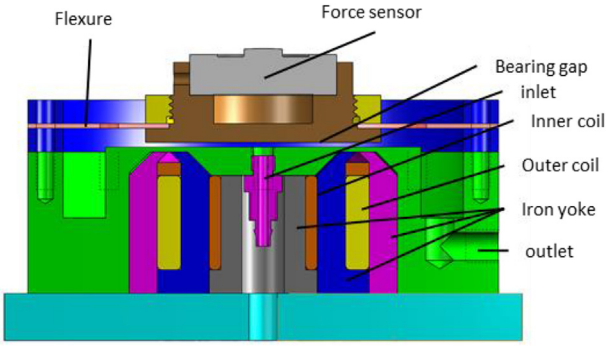

Fig. 5. Schematic of the cross section of the experimental bearing setup.

2.3. Experimental setup

The drawing presented in Fig. 5 presents the experimental setup that mimics the behaviour of the mechanical texturing of Fig. 1. The setup consists of two planar disk-shaped bearing surfaces in which a lubricant enters at the center of the bottom surface and leaves at the edge of the surfaces. Two concentric coils under the bearing surface control the magnetic field strength in the bearing gap. A centrifugal pump (SKF FLM12-2000) pressurizes the fluid to a pressure of $p_p = 5\ bar$. A pressure relief valve (SKF WVN200-10E6) supplies the lubricant at a constant pressure to the system (Fig. 7). The bearing obtains its normal stiffness from a linear restrictor (SKF VD1-105)

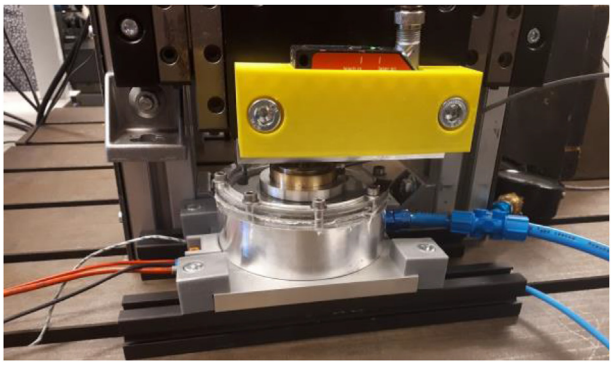

Fig. 6. Picture of the experimental setup.

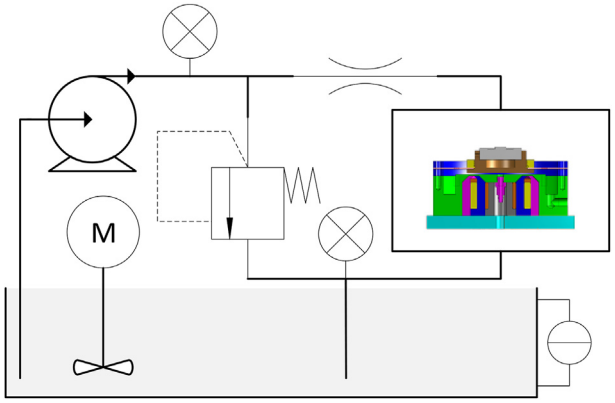

Fig. 7. Hydraulic system used in the experimental setup.

which has a restrictor value of $R_s = 8{,}3 \times 10^{11} Pas/m\hat{}3$ for the lubricant viscosity when no magnetic field is applied. A cylindrical diaphragm flexure suspends the upper bearing surface such that it can move up and down. The flexure is relatively compliant in the tilting direction of the bearing such that it allows self-aligning of the bearing surfaces. The out of plane stiffness of the flexure is much lower than the stiffness of the bearing such that it does not influence the measurements. The upper bearing surface accommodates a FUTEK LLB400-500lb-FSH03891 button-type force sensor. A precise positioning stage pushes against the force sensor from the top such that all applied force flows through the force sensor. A stepper motor controls the stage using a recirculating ball screw to convert the rotational motion onto a translational motion. The optoNCDT1402 laser sensor from Micro-Epsilon measures the height of the bearing gap. The sensor measures the distance between the moving part of the stage and the side rim of the bearing housing (Fig. 6). The stiffness of the force sensor and the construction is much larger than the stiffness of the bearing, so only the stiffness of the bearing is measured. A basic feedback algorithm makes sure that the bearing gap stays at a constant value. The complete system is able to position with a precision of $1\mu m$ and measure the force with a precision of $1N$. Production of the bearing surfaces with a lathe guarantees the smoothness while finishing by polishing guarantees a low surface roughness. The roughness and flatness of the surface are measured with a Bruker ContourGT-K.

The two coils produce a magnetic field in opposite direction such that there is large field at the sides of the bearing and no field in the middle of the bearing. The ratio between the two coils is derived for the situation that there is no magnetic fluid present in the baring gap. Adding a magnetic fluid in the bearing causes the field distribution to change slightly due to the magnetic properties of the fluid. The numerical model takes these effects into account. This makes it possible to validate the shape of the magnetic field by using a Goudsmit HGM09 Gaussmeter. The minimum measured magnetic field intensity in the centre and the maximum field intensity at the sides validate the magnetic field intensity of the numerical model.

The experimental procedure consists of three series of measurements. Table 2 presents the measurement specific parameter values and Table 3 presents the general parameter values of the setup. A measurement series consists of multiple measurements sets. One measurement set consists of one sweep of load capacities measured from high fly height to complete contact between the bearing faces. The first series with a current of $I_0 = 0A$ functions to calibrate and validate the experimental setup. The other two sets function as experimental results of the load characteristic of the hydrostatic bearing with an activated the MR fluid.

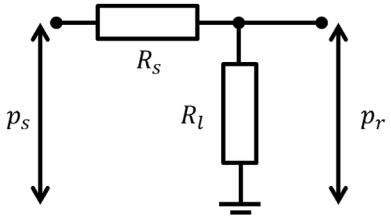

Fig. 8. The pressure in the recess p_r is defined by a potential divider of the restrictor resistance R_s and the land resistance R_l.

2.4. Analytical model

Another paper related to this work and presented in Ref. [25] discusses the analytical model used in the paper extensively. This paper only repeats the important steps in the method. The derivation of the analytical model start from the potential divider of Fig. 8 that makes sure that the bearing systems has stiffness. The linear inlet restrictor R_s and bearing film resistance R_l together define the pressure entering the recess p_r as described by (EQ (7)). The recess pressure finally defines the load capacity of the bearing. The load carrying capacity is calculated for two situations, without and with magnetic field (EQ (7)). is valid for both situations. Figs. 1 and 8, Tables 2 and 3 presents the explanations of the different parameters used.

$$p_r = \frac{R_l}{R_l + R_s} p_s \tag{7}$$

Without the magnetic field, the MR lubricant exhibits no yield stress and thus behaves as a Newtonian fluid. The resistance of a circular hydrostatic bearing as given by (EQ (8)) can reasonable describe the resistance in that situation [47,48].

$$R_l = \frac{6\eta \ln\left(\frac{r_b}{r_0}\right)}{\pi h^3} \tag{8}$$

Substituting (EQ (8)) into (EQ (7)) gives the recess pressure. This result together with the relation given by (EQ (9)) describes the load capacity [47,48].

$$F_{b,\tau_y=0} = \frac{\pi}{2} \frac{(r_b + \Delta r/2)^2 - r_0^2}{\ln\left(\frac{(r_b + \Delta r/2)}{r_0}\right)} p_r \tag{9}$$

Subjecting the MR lubricant to a magnetic field results in a yield stress for the fluid, and thus the fluid behaves as a Bingham plastic fluid. Solving the set of relations presented in (EQ (10)), (EQ (11)) and (EQ (12)) for either $\mathfrak{R}_n$ or p_b results in an analytical expression for the pressure coming out of the restrictor. These relations are taken from the related work presented in Ref. [25]. These relations practically include the effect of having a plug in the middle of the flow caused by the yield stress of the fluid. Relation (EQ (11)) uses the assumption of modelling the resistance of the bearing by a slit with a length of Δr at a radial distance of r_b. The contribution of the resistance of the inner section (recess) where there is negligible magnetic field is neglected.

$$p_s = \frac{2\tau_y}{h} \frac{\Delta r}{\mathfrak{R}_n} \left(1 + \frac{R_s}{2R_\infty}(2 - 3\mathfrak{R}_n + \mathfrak{R}_n^3)\right) \tag{10}$$

$$R_\infty = \frac{12\eta\Delta r}{Lh^3} = \frac{12\eta\Delta r}{\pi r_b h^3} \tag{11}$$

$$\mathfrak{R}_n = \frac{2\tau_y}{h} \frac{\Delta r}{p_r} \tag{12}$$

The pressure consequently goes down from the point $r_b - \Delta r/2$ till the edge of the bearing defined by $r_b + \Delta r/2$. The leads to the following relation for the load capacity:

$$F_{b,\tau_y\neq 0} = \frac{\pi}{2}\frac{(r_b + \Delta r/2)^2 - (r_b - \Delta r/2)^2}{\ln\left(\frac{r_b+\Delta r/2}{r_b-\Delta r/2}\right)} p_r \tag{13}$$

2.5. Numerical model

The numerical model package COMSOL Multiphysics 5.3a is used to develop a finite element model of the bearing system. This work again follows the same procedure as presented in the related work [25]. The axisymmetric design of the setup facilitates an axisymmetric numerical model. The first step in the modelling is calculating the magnetic field followed by a flow calculation. Section 2.2 presents the specifications of the magnetic properties and the method of validating the field. This magnetic field functions as an input for the flow calculation since it defines the yield stress of the material. A Stokes flow models the flow of the fluid. The walls of the channel have a zero slip boundary condition. An input pressure in function of the flow that flows through the bearing defines the behaviour of the linear restrictor as presented in (EQ (14)).

$$p_r = p_{in} - Q_{out} R_s \tag{14}$$

A zero pressure condition defines the output of the flow at the outside rim of the bearing surfaces. Section 2.2 presents the properties of the fluid used in the model. The free triangular mesh is very small at the walls in order to account for the high shear gradient expected at the walls due the expected large size of the plug. The maximum size of the element near the walls scale such that enough elements are present to model the behaviour of the fluid. In addition, the use of P3 + P2 elements (third order velocity and second order pressure) increases the form freedom of the elements near the walls. A nonlinear solver accommodates for the nonlinear behaviour of the fluid. Numerical iterations both for the magnetic field and for the flow field are continued until a relative tolerance of 10^{-4} on the residual is reached. The modelling results consists of three series. Table 2 presents the measurement specific parameter values and Table 3 presents the general parameter values of the setup. Computations are done on an Intel Xeon CPU E5-1620 V3 @ 3.50 GHz with 32 GB of Ram.

3. Results

Fig. 9 presents the magnetic field distribution over the radius of the bearing in the presence of a magnetic fluid. The distribution has a minimum in the centre of the bearing and a maximum at the outer radius of the bearing. Table 4 presents the measurements with the Teslameter on the experimental setup without a magnetic fluid present. Again, a minimum is present in the centre and a maximum is present at the outer radius. The minima and maxima present in the measurement compare well with those in the numerical model, and this validates the magnetic field used in the numerical model.

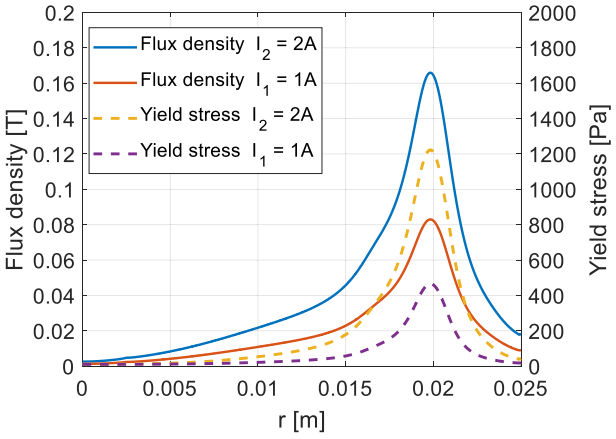

Fig. 9. Magnetic field without a magnetic fluid present in the bearing gap. The solid line presents the magnetic field at a fly height of $h = 0.1\ mm$ and the dashed line presents the corresponding yield stress.

Table 4
Magnetic flux density measured on the experimental setup without a magnetic fluid present.

Current	Measured flux density centre	Measured flux density side
$I_1 = 1A$	$B_{cent,1} = 3mT$	$B_{side,1} = 57mT$
$I_2 = 2A$	$B_{cent,2} = 7mT$	$B_{side,2} = 132mT$

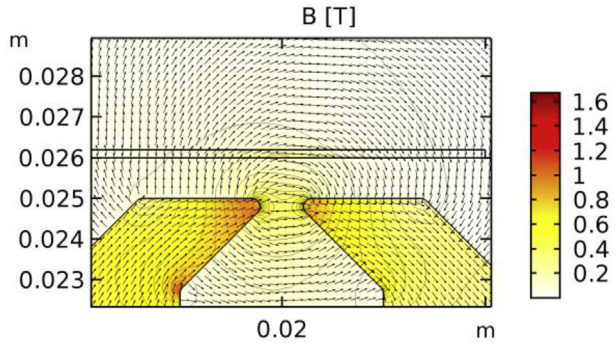

Fig. 10. Plot of the magnetic field produced in the system. The arrows have a normalized size.

Fig. 9 also presents the yield stress distribution over the radius of the bearing film for the two different field intensities investigated while there is a magnetic field present in-between the two bearing faces. Fig. 10 presents the flow of the flux in the system. Note that within the bearing gap, the flux flows radially, either inwards or outwards. The realised shape of the magnetic field resembles the mechanical equivalent of Fig. 1.

Fig. 11 presents the first measurement series in the absence of a magnetic field. The graph shows both the raw measurements, the predicted analytical model and the fitted model. The measurements and the predicted analytical model show an offset in force. A correction factor of $f_{fit,force} = 0.9$ has been applied in the fitted model, demonstrating the accurate trend of the predicted model. This shows that the model is about 10% off. The other measurements do not make use of this fitting factor.

Fig. 13 and Fig. 14 present respectively the results of measurement

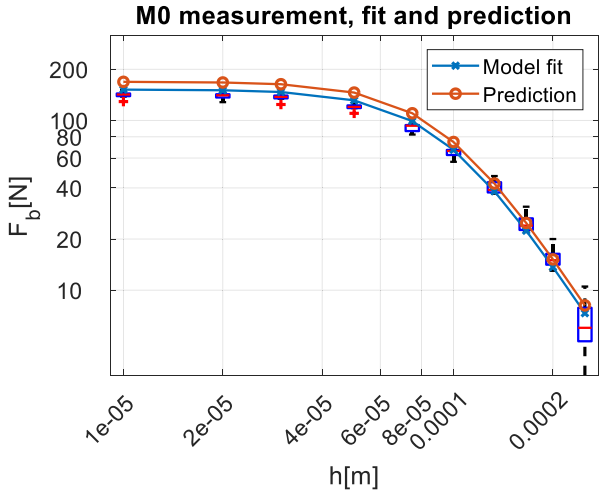

Fig. 11. Load capacity of the bearing in the absence of a magnetic field. The graph shows both the measurements, the predicted model and the fitted model. The boxplots presents the measured data.

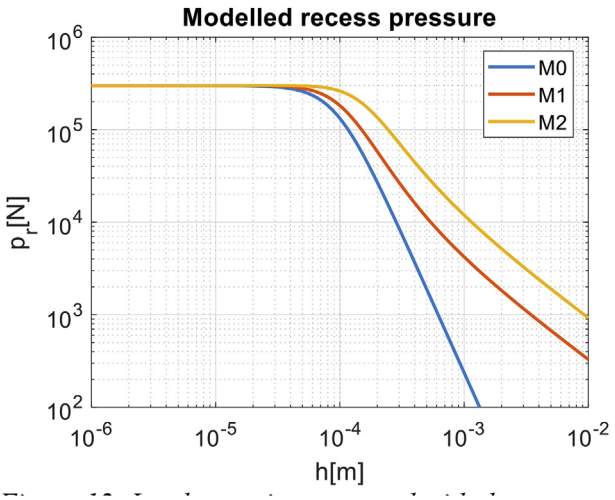

Fig. 12. Load capacity generated with the parameters used in the different graphs.

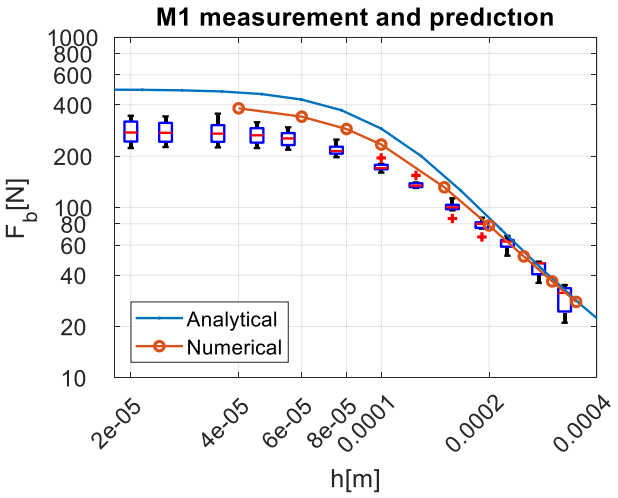

Fig. 13. Load capacity of the bearing in situation M1.

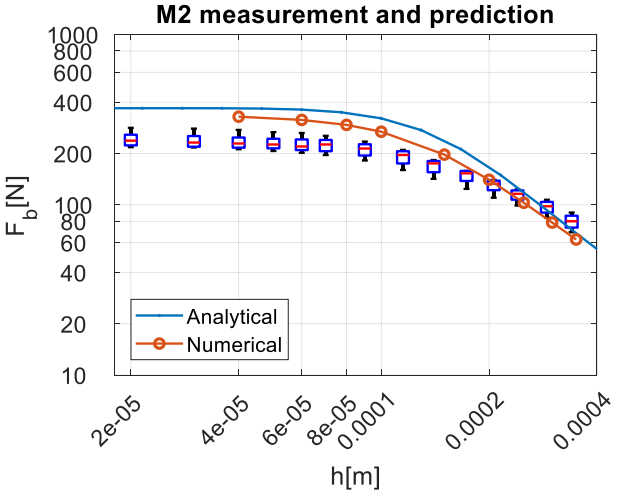

Fig. 14. Load capacity of the bearing in situation M2.

condition M1 and M2 presented in Table 2. The different boxplots present the different performed measurements. The solid line presents the analytical model and the line with circles presents the results from the numerical model. Fig. 12 presents the three analytical models

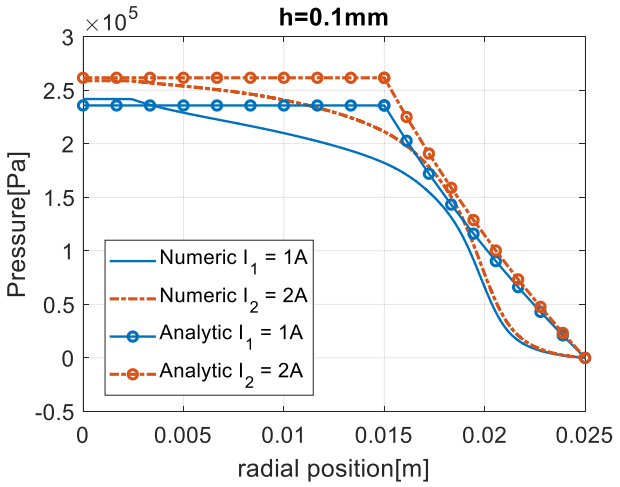

Fig. 15. Pressure distribution in the bearing film over the radius of the bearing for a film height of $h = 0.1mm$.

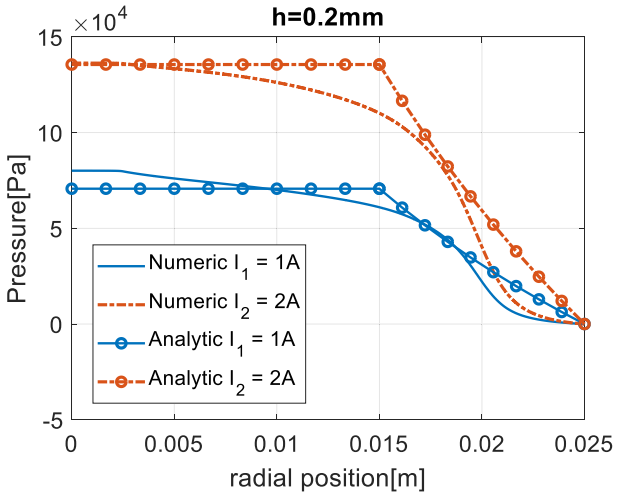

Fig. 16. Pressure distribution in the bearing film over the radius of the bearing for a film height of$h = 0.2mm$.

discusses in this paper for a wider range of film heights and a constant pressure source, all other parameter values are the same as elsewhere in this paper. Fig. 15 and Fig. 16 presents the pressure distribution in between the bearing surfaces the situation of $I_1 = 1A$ and $I_2 = 2A$ for respectively a film height of h= 0.2mm and h= 0.1mm. Note that the difference between the two situations presented in Fig. 15 is only small due to the difference in source pressure.

4. Discussion

The discussion of this paper first discusses the individual measurements done in this research. It does this by interpreting the individual measurements, analysing the validity and possible relating them to other work. The discussion ends with a general discussion the similarities of a hydrostatic bearing using only geometrical surface textures and a hydrostatic bearing using only MR textures.

The viscous model presented in Fig. 3seems to overestimate the viscous behaviour of the fluid at lower shear rates ($\dot{\gamma} < 100$). This introduces some error when the flow rates are small resulting in modelling a more viscous fluid than actually is the case. The spread in the viscous behaviour presented in Fig. 4 shows to be very large at high magnetic flux densities. This has no significant effects on the results of the numerical model since the maximum field strength present in the fluid stays well under the $0{,}2T$ as can be seen from Fig. 9. Fig. 9

furthermore shows that there is no proportional relation between the yield stress of the fluid and the flux density present. Most of the yield stress is present at the sides of the bearing.

The properties measured with the cone-plate rheometer only measures the fluid properties in the direction tangent to the shear rate and tangent to the speed of the flow. Research showed that the rheological properties are lower in the other two orthogonal direction [49–55]. Applying a magnetic field to an MR fluid causes pillars of magnetic particles to form in the fluid aligning with the magnetic field [56,57]. The work of [51,52] demonstrates that the yield stress can differ as much as a factor 5 in different directions due to this effect. Fig. 10 shows that most of the field is perpendicular to the bearings surfaces but some part of the field (that is near the peak of the field) is parallel to the bearing surfaces. This results in the situation that the resulting yield strength and viscosity near that peak are in reality lower than assumed in the numerical and analytical model. Since the magnetic field in this research is relatively uniform, the effect of the anisotropic behaviour is relatively small. The effect can be large in other systems that do not have a uniform magnetic field; there the anisotropy should be included into the calculations to have accurate representation of the system.

The data presented in Fig. 11 shows a slight offset of 10% between the measured load capacity and the modelled load capacity. This inaccuracy is probably due to some inaccuracies in the experimental setup. Some possible inaccuracies are for example the value of the linear restrictor, the flatness and parallelism of the bearing faces and the hysteresis of the pressure control valve. The magnitude of this error demonstrates that the setup in itself is working properly.

The data presented in Figs. 13 and 14 show a good accordance at higher fly heights. Both the analytical model and the numerical model are well within the inaccuracy of the measurements. The difference between the numerical model and analytical model is larger for a current of $I_2 = 2A$ than for a current of$I_1 = 1A$. Fig. 16 presents a reason for this difference by presenting the pressure distribution of the radius of the bearing for the film height of $h = 0.2mm$. The graph shows that pressure distributions calculated numerically and analytically show more difference in the situation of $I_2 = 2A$ than in the situation of $I_1 = 1A$. This leads to a larger difference in load in the situation of $I_2 = 2A$ than in the situation of $I_1 = 1A$.

The pressure distributions presented in Figs. 15 and 16 show a clear decline in pressure at the locations where the field intensity is high. Still a small decline in pressure is visible where the field strength is small which means that the viscosity in the absence of a magnetic field still causes a significant resistance. These losses are not taken into account in the analytical model, which is the main reason of the differences between the analytical and numerical model. The losses in the absence of a magnetic field can be included in the analytical model but then the big advantage of a simple insightful model is lost.

Offsets between the analytical models, the numerical models and the experimental measurements are large at lower fluid film heights. This indicates that some inaccuracies are present in the pressure distribution over the radius of the bearing. An error in the resistance of the bearing itself is not likely since the resistance does not significantly influence the load capacity at low fly heights. Fig. 15 shows that the pressure distribution assumed in the analytical model is a less good fit to the numerical calculated pressure distribution when compared to the data presented in Fig. 16. The difference between the calculations and the measurements is probably due to the assumption of the Bingham plastic material model. Fig. 3shows that the difference of the assumed fluid model and the measured fluid model is larger for relatively low shear rates compared to the measured values. The shear rates become lower for lower fluid film heights since both the fluid speed and film height decreases. This causes an error in the yield stress in that situation. This error is larger at the sides of the bearing than in the centre of the bearing since the plug is larger at the sides due to the lower speed there. This results in the situation that the effect of an overestimated yield stress is especially significant at the sides of the bearing. This means that the pressure should decline faster in radial direction than is currently assumed. A faster declining pressure eventually results in a lower load capacity. This situation might be resolved by using the Herschel-Bulkley model.

Fig. 12 shows the recess pressure calculated with the analytical model for a wider range of fluid film height and the same pressure source. These lines show the effect of applying a magnetic field to the system at a larger scale.

The analytical model is a good addition in the analyses of hydrostatic bearings lubricated with MR fluids. The model might be less accurate compared to the numerical model, but it way less computational demanding. The total computation time of the numerical model is 5.5 h while the total computation time of all other calculations for this research only took a few seconds. This makes is possible to check quickly the effect of certain parameters and the simplicity of the model facilitates the development of some insight into the effects of certain parameters.

In general, the research stated that a hydrostatic bearing with MR structure mimics the behaviour of a hydrostatic bearing with geometrical surface textures. The experimental setup present in this research has only two flat bearing surfaces, a resistance at the outer sides of the bearing surfaces is created by using a MR fluid and applying a magnetic field at the outer locations of the bearing. Figs. 16 and 15 show pressure distributions that are similar to the one found in conventional hydrostatic bearings with geometrical surface textures. The behaviour is similar but not the same since the resistance of a MR structure scales different with the fluid film height and applied pressure compared to a geometrical surface texture as can be seen from Fig. 12.

The magnetic field effects the flow in a similar way as does the geometry of the bearing. This means that for a computation, the shape of the magnetic field should be treated the same as the shape of the geometry of the bearing. This means that both the geometry and the shape of the magnetic field function as inputs of the flow modelling in the bearing.

Interesting to note is that the theory presented in this research is also applicable to hydrostatic bearings lubricated with a Bingham plastic lubricant. A hydrostatic bearing configuration using a geometrical texture as a resistance at the sides of the bearing faces shall show a similar bearing stiffness as the one presented here.

5. Conclusions

This research presents the load characteristic of a hydrostatic bearing using MR structures by means of an experimental setup, a numerical model and an analytical model. The research demonstrates that a local magnet together with a magnetorheological fluid generates similar effects as a local decrease in fluid film height. Similar but not identical since the resistance scales different compared to a change in fluid film height and applied pressure.

The three different models give characteristics that are in the same order of magnitude which means that they are useful in the design of a hydrostatic bearing lubricated with magnetorheological fluids. The analytical model is the coarsest but has as advantage that it is very quick to calculate. The numerical model is more precise but suffer from the fact that the computation is very demanding. The main reason for the inaccuracy of the analytical model are the coarse assumptions. The inaccuracy of the computation model is the result of an inaccurate material model. Furthermore, interesting to note is that the theory is also applicable for any other lubricant that behaves as a Bingham plastic.

Acknowledgement

The Dutch TKI maritime funding program has supported this research.

Appendix A. Supplementary data

Supplementary data to this article can be found online at https://doi.org/10.1016/j.cap.2019.09.004.

References

[1] S.S. Perry, W.T. Tysoe, Frontiers of fundamental tribological research, Tribol. Lett. 19 (3) (2005) 151–161.
[2] N.K. Myshkin, I.G. Goryacheva, Tribology: trends in the half-century development, J. Frict. Wear 37 (6) (2016) 513–516.
[3] K. Holmberg, A. Erdemir, Influence of tribology on global energy consumption, costs and emissions, Friction 5 (3) (2017) 263–284.
[4] S.G.E. Lampaert, J.W. Spronck, R.A.J. van Ostayen, Load and stiffness of a planar ferrofluid pocket bearing, Proc. Inst. Mech. Eng. J J. Eng. Tribol. 232 (1) (2017) 14–25.
[5] S.G.E. Lampaert, B.J. Fellinger, J.W. Spronck, R.A.J. van Ostayen, In-plane friction behaviour of a ferrofluid bearing, Precis. Eng. 54 (2018) 163–170.
[6] M. Holmes, D. Trumper, Magnetic/fluid-bearing stage for atomic-scale motion control (the angstrom stage), Precis. Eng. 18 (1) (1996) 38–49.
[7] W. Ochonski, Sliding bearings lubricated with magnetic fluids, Ind. Lubr. Tribol. 59 (6) (2007) 252–265.
[8] H. Urreta, Z. Leicht, A. Sanchez, A. Agirre, P. Kuzhir, G. Magnac, Hydrodynamic bearing lubricated with magnetic fluids, J. Intell. Mater. Syst. Struct. 21 (15) (2010) 1491–1499.
[9] X. Wang, H. Li, G. Meng, Rotordynamic coefficients of a controllable magnetorheological fluid lubricated floating ring bearing, Tribol. Int. 114 (April) (2017) 1–14.
[10] J. Hesselbach, C. Abel-Keilhack, Active hydrostatic bearing with magnetorheological fluid, Proc. Eighth Int. Conf. New Actuators, 2002, pp. 343–346.
[11] J. Hesselbach, C. Abel-Keilhack, Active hydrostatic bearing with magnetorheological fluid, J. Appl. Phys. 93 (10) (2003) 8441–8443.
[12] J.M. Guldbakke, C. Abel-Keilhack, J. Hesselbach, Magnetofluidic bearings and dampers J.M. Colloidal Magnetic Fluids : Basics, Development and Application of Ferrofluids, 2009.
[13] D. Brousseau, E.F. Borra, M. Rochette, D.B. Landry, Linearization of the response of a 91-actuator magnetic liquid deformable mirror, Opt. Express 18 (8) (2010) 8239–8250.
[14] D.A. Bompos, P.G. Nikolakopoulos, Rotordynamic analysis of a shaft using magnetorheological and nanomagnetorheological fluid journal bearings, Tribol. Trans. 59 (1) (2016) 108–118.
[15] D.A. Bompos, Tribological Design of Nano/Magnetorheological Fluid Journal Bearings, (2015).
[16] D.A. Bompos, P.G. Nikolakopoulos, CFD simulation of magnetorheological fluid journal bearings, Simul. Model. Pract. Theory 19 (4) (2011) 1035–1060.
[17] N. Vaz, et al., Experimental investigation of frictional force in a hydrodynamic journal bearing lubricated with magnetorheological fluid, J. Mech. Eng. Autom. 7 (5) (2017) 131–134.
[18] A. Bouzidane, M. Thomas, An electrorheological hydrostatic journal bearing for controlling rotor vibration, Comput. Struct. 86 (3–5) (2008) 463–472.
[19] O.-O. Christidi-Loumpasefski, I. Tzifas, P.G. Nikolakopoulos, C.A. Papadopoulos, Dynamic analysis of rotor – bearing systems lubricated with electrorheological fluids, Proc. Inst. Mech. Eng. - Part K J. Multi-body Dyn. 0 (0) (2017) 1–16.
[20] J.S. Basavaraja, S.C. Sharma, S.C. Jain, A study of misaligned electrorheological fluid lubricated hole-entry hybrid journal bearing, Tribol. Int. 43 (5–6) (2010) 1059–1064.
[21] S.C. Sharma, C.B. Khatri, Electro-rheological fluid lubricated textured multi-lobe hole-entry hybrid journal bearing system, J. Intell. Mater. Syst. Struct. 29 (8) (2018) 1600–1619.
[22] S.G.E. Lampaert, R.A.J. van Ostayen, Virtual textured hybrid bearings, 44th Leeds-Lyon Symposium on Tribology, 2017, p. 84.
[23] S.G.E. Lampaert, R.A.J. Van Ostayen, Hydrostatic bearing with MR texturing, Book of Abstracts 16th German Ferrofluid Workshop, 2017, pp. 94–95.
[24] S.G.E. Lampaert, R.A.J. van Ostayen, Predicting the behaviour of magnetorheological textured bearings, The 18th Nordic Symposium on Tribology – NORDTRIB 2018, 2018.
[25] S.G.E. Lampaert, R.A.J. van Ostayen, Load and stiffness of a hydrostatic bearing lubricated with a Bingham plastic fluid, J. Intell. Mater. Syst. Struct. (2019), https://doi.org/10.1177/1045389X19873426.
[26] S.G.E. Lampaert, R.A.J. van Ostayen, Lubricated Sliding Bearing with Adjustment of the Properties of the Lubricant in Certain Parts of the Bearing Gap, WO2018212657, 2018.
[27] M. Ashtiani, S.H. Hashemabadi, A. Ghaffari, A review on the magnetorheological fluid preparation and stabilization, J. Magn. Magn. Mater. 374 (2015) 711–715.
[28] S.R. Gorodkin, R.O. James, W.I. Kordonski, Magnetic properties of carbonyl iron particles in magnetorheological fluids, J. Phys. Conf. Ser. 149 (2009) 012051.
[29] V.A. Markel, Introduction to the Maxwell garnett approximation: tutorial, J. Opt. Soc. Am. A 33 (7) (2016) 1244.
[30] A.C. Becnel, S. Sherman, W. Hu, N.M. Wereley, Nondimensional scaling of magnetorheological rotary shear mode devices using the Mason number, J. Magn. Magn. Mater. 380 (2015) 90–97.
[31] K. Danas, S.V. Kankanala, N. Triantafyllidis, Experiments and modeling of iron-particle-filled magnetorheological elastomers, J. Mech. Phys. Solids 60 (1) (2012) 120–138.
[32] D. Szabo, M. Zrinyi, Nonhomogeneous, non-linear deformation of polymer gels swollen with magneto-rheological suspensions, Int. J. Mod. Phys. B 16 (17–18) (2002) 2616–2621.
[33] M. Chand, A. Shankar, Noorjahan, K. Jain, R.P. Pant, Improved properties of bi-dispersed magnetorheological fluids, RSC Adv. 4 (96) (2014) 53960–53966.
[34] A. Ghaffari, S.H. Hashemabadi, M. Ashtiani, A Review on the Simulation and Modeling of Magnetorheological Fluids vol. 26, (2015), pp. 881–904 8.
[35] J.L. Arias, V. Gallardo, F. Linares-Molinero, A.V. Delgado, Preparation and characterization of carbonyl iron/poly(butylcyanoacrylate) core/shell nanoparticles, J. Colloid Interface Sci. 299 (2) (2006) 599–607.
[36] A. J. F. Bombard, I. Joekes, and M. Knobel, "Magnetic Susceptibility and Magnetic Hysteresis Loop of Some Carbonyl Iron Powders Used in Magnetorheological Fluids, " pp. 1–6.
[37] M.A. Abshinova, S.M. Matitsine, L. Liu, C.R. Deng, L.B. Kong, High microwave magnetic permeability of composites with submicron iron flakes, J. Phys. Conf. Ser. 266 (1) (2011) 6–11.
[38] M.T. López-López, J. de Vicente, G. Bossis, F. González-Caballero, J.D.G. Durán, Preparation of stable magnetorheological fluids based on extremely bimodal iron–magnetite suspensions, J. Mater. Res. 20 (04) (2005) 874–881.
[39] P. Kim, J.I. Lee, J. Seok, Analysis of a viscoplastic flow with field-dependent yield stress and wall slip boundary conditions for a magnetorheological (MR) fluid, J. Nonnewton. Fluid Mech. 204 (2014) 72–86.
[40] T.C. Papanastasiou, Flows of materials with yield, J. Rheol. (N. Y. N. Y). 31 (5) (1987) 385–404.
[41] D.N. Smyrnaios, J.A. Tsamopoulos, Squeeze flow of Bingham plastics, J. Nonnewton. Fluid Mech. 100 (1–3) (2001) 165–190.
[42] P. Coussot, Yield stress fluid flows: a review of experimental data, J. Nonnewton. Fluid Mech. 211 (2014) 31–49.
[43] M. Dinkgreve, J. Paredes, M.M. Denn, D. Bonn, "On different ways of measuring 'the' yield stress, J. Nonnewton. Fluid Mech. 238 (2016) 233–241.
[44] J.C. Lambropoulos, C. Miao, S.D. Jacobs, Magnetic field effects on shear and normal stresses in magnetorheological finishing, Opt. Express 18 (19) (2010) 19713–23.
[45] H.M. Laun, C. Kormann, N. Willenbacher, Rheometry on magnetorheological (MR) fluids, Rheol. Acta 35 (5) (1996) 417–432.
[46] M. Zubieta, S. Eceolaza, M.J. Elejabarrieta, M.M. Bou-Ali, Magnetorheological fluids: characterization and modeling of magnetization, Smart Mater. Struct. 18 (9) (2009).
[47] G.W. Stachowiak, A.W. Batchelor, Engineering Tribology, fourth ed., Elsevier Inc., 2014.
[48] R. Van Ostayen, "The Hydro–Support: an Elasto–Hydrostatic Thrust Bearing with Mixed Lubrication, (2002).
[49] H. Wang, C. Bi, J. Kan, C. Gao, W. Xiao, The mechanical property of magnetorheological fluid under compression, elongation, and shearing, J. Intell. Mater. Syst. Struct. 22 (8) (2011) 811–816.
[50] P. Kuzhir, et al., Magnetorheological effect in the magnetic field oriented along the vorticity, J. Rheol. (N. Y. N. Y). 58 (6) (2014) 1829–1853.
[51] E. Dohmen, N. Modler, M. Gude, Anisotropic characterization of magnetorheological materials, J. Magn. Magn. Mater. 431 (2017) 107–109.
[52] E. Dohmen, D. Borin, A. Zubarev, Magnetic field angle dependent hysteresis of a magnetorheological suspension, J. Magn. Magn. Mater. 443 (2017) 275–280.
[53] P. Kuzhir, G. Bossis, V. Bashtovoi, O. Volkova, Effect of the orientation of the magnetic field on the flow of magnetorheological fluid. II. Cylindrical channel, J. Rheol. (N. Y. N. Y). 47 (6) (2003) 1385.
[54] P. Kuzhir, G. Bossis, V. Bashtovoi, Effect of the orientation of the magnetic field on the flow of a magnetorheological fluid. I. Plane channel, J. Rheol. (N. Y. N. Y). 47 (6) (2003) 1373–1384.
[55] J. Takimoto, H. Takeda, Y. Masubuchi, K. Koyama, Stress rectification in MR fluids under tilted magnetic field, Int. J. Mod. Phys. B 13 (14, 15 & 16) (1999) 2028–2035.
[56] H.E. Horng, C. Hong, S.Y. Yang, H.C. Yang, Novel properties and applications in magnetic fluids, J. Phys. Chem. Solids 62 (2001) 1749–1764.
[57] C.-Y. Hong, Field-induced structural anisotropy in magnetic fluids, J. Appl. Phys. 85 (8) (1999) 5962–5964.